

Riemannian Motion Generation

A Unified Framework for Human Motion Representation and Generation via Riemannian Flow Matching

Fangran Miao¹ Jian Huang^{1,2}✉ Ting Li³✉ *

¹Department of Data Science and Artificial Intelligence, The Hong Kong Polytechnic University

²Department of Applied Mathematics, The Hong Kong Polytechnic University

³Department of Data Science and Statistics, Southern University of Science and Technology

✉Corresponding Author

🔗Project Page

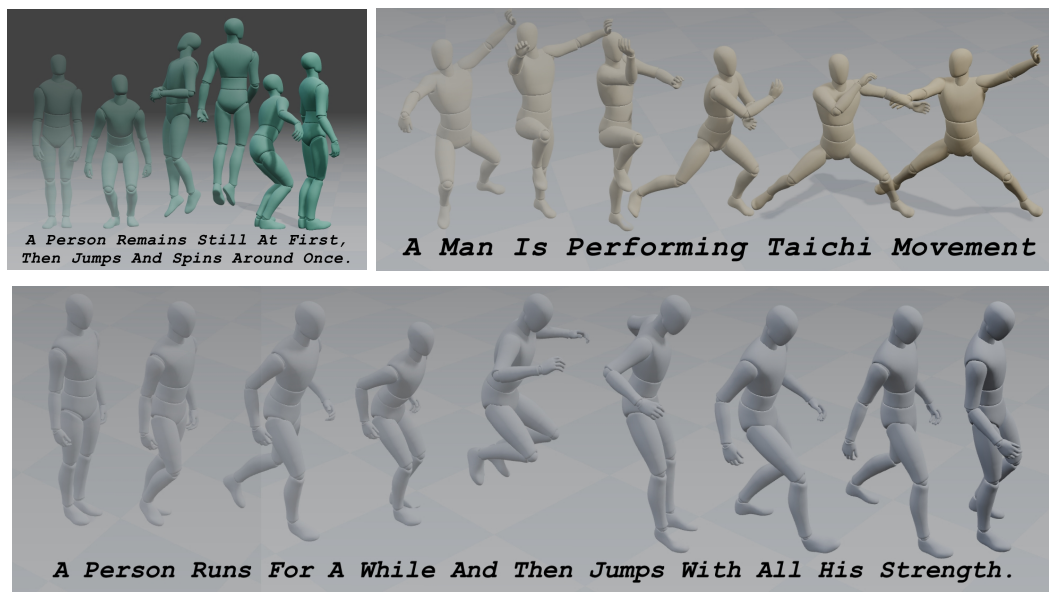


Figure 1: Text-to-motion samples under our **Riemannian Motion Generation** framework.

Abstract

Human motion generation is often learned in Euclidean spaces, although valid motions follow structured non-Euclidean geometry. We present **Riemannian Motion Generation (RMG)**, a unified framework that represents motion on a product manifold and learns dynamics via Riemannian flow matching. RMG factorizes motion into several manifold factors, yielding a scale-free representation with intrinsic normalization, and uses geodesic interpolation, tangent-space supervision, and manifold-preserving ODE integration for training and sampling. On HumanML3D, RMG achieves state-of-the-art FID in the HumanML3D format (0.043) and ranks first on all reported metrics under the MotionStreamer format. On MotionMillion, it also surpasses strong baselines (FID 5.6, R@1 0.86). Ablations show that the compact $\mathcal{T} + \mathcal{R}$ (translation + rotations) representation is the most stable and

*Email: fangran.miao@connect.polyu.hk, j.huang@polyu.edu.hk, liting@sustech.edu.cn

effective, highlighting geometry-aware modeling as a practical and scalable route to high-fidelity motion generation.

1 Introduction

Conditional human motion generation has emerged as a key challenge in generative modeling, incorporating conditioning signals that range from text descriptions and action labels to audio, music, and scene context [Zhu et al., 2024]. Synthesizing high-fidelity motion sequences is essential for advancements in human-computer interaction, embodied AI, and augmented-reality content creation.

Recent progress in human motion generation has primarily focused on model architecture. While earlier methods relied on VAEs (e.g., TEMOS [Petrovich et al., 2022] and T2M [Guo et al., 2022]), state-of-the-art systems increasingly adopt diffusion or autoregressive frameworks [Zhang et al., 2024, Tevet et al., 2022, Xiao et al., 2025, Guo et al., 2025, Kim et al., 2023, Guo et al., 2024, Zhang et al., 2023, Jiang et al., 2023]. By contrast, the geometry of motion representation has received less systematic attention, despite its direct impact on optimization difficulty, sampling stability, and physical plausibility.

Most existing pipelines still encode motion using redundant Euclidean coordinates, enforcing validity only implicitly through constraints or post-processing. For a skeleton with J joints, an articulated pose has intrinsic degrees of freedom on the order of $3J$; however, common encodings concatenate multiple correlated views of the same state, occupying a much higher-dimensional ambient space. Table 1 summarizes these encoding strategies across previous methods. Consequently, models are trained in \mathbb{R}^D , whereas physically valid motions reside on, or near, a lower-dimensional manifold with intrinsic dimension d .

This observation suggests a simple but important motivation: if data already resides on a lower-dimensional manifold and follows a strong geometric structure, the generative models should benefit from operating in that space and respect that structure rather than in an unconstrained ambient vector space. Our key insight is that much of the apparent complexity of human motion does not come from arbitrary high-dimensional variation, but from composing several low-dimensional factors, each with its own natural geometry. Once this factorization is made explicit, geometric consistency no longer needs to be imposed only after generation. Instead, it can be built directly into both the representation and the generative dynamics. This viewpoint naturally leads to a geometry-aware formulation in which representation and model design are developed together, rather than treated as separate concerns.

Guided by this perspective, we first provide a unified geometric view that decomposes existing representations into common factors and their natural manifolds. Building on this view, we introduce **Riemannian Motion Generation (RMG)**, a representation-and-generation framework that models motion on a product manifold and learns dynamics via Riemannian flow matching. RMG yields a compact manifold-aware parameterization and a geometry-consistent training/inference pipeline. On HumanML3D text-to-motion benchmarks, it matches or exceeds strong baselines across quality, alignment, and diversity metrics. Moreover, RMG surpasses all baselines on the large-scale MotionMillion dataset, demonstrating superior scalability and generalization.

We summarize our core contributions as follows:

- We propose **Riemannian Motion Generation (RMG)**, a geometric paradigm for human motion generation that models motion on product manifolds and learns dynamics via Riemannian flow matching.
- We design a compact Riemannian representation that is both effective and efficient, and we provide a systematic evaluation of representation geometry in the context of human motion generation.
- To the best of our knowledge, we present the first demonstration that Riemannian flow matching scales effectively to large datasets and modern high-capacity generative architectures.
- We demonstrate strong empirical results on text-to-motion benchmarks, showing consistent gains across quality, alignment, and diversity metrics.

Table 1: Comparison of motion representations. \mathcal{T} : global translation; $\mathcal{R}_{\text{Orientation}}$: global orientation; $\mathcal{R}_{\text{Joint}}$: per-joint rotation; \mathcal{P} : joint position; d: temporal difference of the variable. Compared to existing formats, our method adopts the most concise format, with each factor represented on its natural manifold.

| Format | \mathcal{T} | $\mathcal{R}_{\text{Orientation}}$ | $\mathcal{R}_{\text{Joint}}$ | \mathcal{P} | d \mathcal{T} | d $\mathcal{R}_{\text{Orientation}}$ | d $\mathcal{R}_{\text{Joint}}$ | d \mathcal{P} | Foot Contact | Ambient Dimension |
|----------------|---------------|------------------------------------|------------------------------|---------------|-----------------|--------------------------------------|--------------------------------|-----------------|--------------|-------------------|
| HumanML3D | \times | \times | \checkmark | \checkmark | \checkmark | \checkmark | \times | \checkmark | \checkmark | $12J - 1$ |
| MotionStreamer | \times | \times | \checkmark | \checkmark | \checkmark | \checkmark | \times | \checkmark | \times | $12J + 8$ |
| DART | \checkmark | \checkmark | \checkmark | \checkmark | \checkmark | \checkmark | \times | \checkmark | \times | $12J + 12$ |
| HY-Motion | \checkmark | \checkmark | \checkmark | \checkmark | \times | \times | \times | \times | \times | $9J + 3$ |
| RMG (Ours) | \checkmark | \checkmark | \checkmark | \times | \times | \times | \times | \times | \times | $4J + 3$ |

2 Related Works

2.1 Human Motion Generation

Human motion generation has witnessed rapid progress, propelled by improvements in deep learning and motion capture technologies. Early approaches primarily adopted regression models to map predefined action labels to motion sequences, exemplified by works such as Action2Motion [Guo et al., 2020] and SA-GAN [Yu et al., 2020]. The introduction of advanced generative models—including Variational Autoencoders [Petrovich et al., 2021, Kingma et al., 2013], Generative Adversarial Networks [Degardin et al., 2022, Goodfellow et al., 2014], normalizing flows [Rezende and Mohamed, 2015, Valle-Pérez et al., 2021], and more recently, diffusion models [Tevet et al., 2022, Petrovich et al., 2021, Chen et al., 2023, Tseng et al., 2023, Kim et al., 2023, Dabral et al., 2023] has enabled the modeling of complex, multi-modal motion distributions and the synthesis of more realistic and diverse human motions.

A significant trend in recent years is the use of conditional generative models, where motion is synthesized based on various forms of contextual signals [Petrovich et al., 2022, Kim et al., 2022, Tevet et al., 2022, Guo et al., 2020, Petrovich et al., 2022, Zhang et al., 2023, Li et al., 2021, Ao et al., 2022]. These methods have evolved from simple mappings to architectures that exploit joint embeddings, transformers [Petrovich et al., 2022, Guo et al., 2020], and diffusion processes [Tevet et al., 2022, Tseng et al., 2023, Dabral et al., 2023, Chen et al., 2023], resulting in higher fidelity and controllable motion sequences.

Despite these advances, human motion generation remains challenging due to the highly articulated and nonlinear nature of human movement, as well as the need for semantic alignment with conditioning signals. Evaluation protocols are still evolving, with a combination of objective metrics and user studies commonly employed to assess the naturalness, diversity, and consistency of generated motions [Guo et al., 2022, Tevet et al., 2022, Petrovich et al., 2021, Chen et al., 2021, Huang et al., 2020, Liu et al., 2022a].

2.2 Riemannian Manifold

A smooth manifold \mathcal{M} [Lee, 2012] is a topological space that locally resembles Euclidean space \mathbb{R}^n , which allows for the application of calculus, and it becomes a *Riemannian manifold* (\mathcal{M}, g) when it is endowed with a Riemannian metric g [Lee, 2018]. The metric is a smoothly varying inner product on each tangent space, defining the inner product between any two tangent vectors $u, v \in T_p\mathcal{M}$ as $g_p(u, v)$. This structure allows for the measurement of geometric properties, such as the length of a vector, and the angle between vectors. The metric also induces a distance function on the manifold, typically the geodesic distance, which measures the length of the shortest path between two points [Lee, 2018].

Furthermore, the Riemannian metric defines a canonical volume form dV , which is essential for integration and defining probability distributions on the manifold [Lee, 2018]. A probability density function $f : \mathcal{M} \rightarrow \mathbb{R}^+$ must satisfy the normalization condition $\int_{\mathcal{M}} f(p) dV(p) = 1$. This has enabled the development of statistical models on non-Euclidean domains, such as the Riemannian uniform/normal distribution, which are crucial for modern data analysis as well as the generative modeling on the Riemannian manifold [Pennec, 2006, Said et al., 2017].

2.3 General Flow Matching

Flow matching [Lipman et al., 2022, Albergo et al., 2023, Liu et al., 2022b], combining aspects from Continuous Normalizing Flows and Diffusion Models, learns a time-dependent velocity field that transports a source distribution p_0 to a target distribution p_1 . A standard training objective is the conditional flow-matching loss:

$$\mathcal{L}_{\text{CFM}}(\theta) = \mathbb{E}_{t, \mathbf{x}_1, \mathbf{x}_t} \|v_t(\mathbf{x}_t | \mathbf{x}_1) - v_\theta(\mathbf{x}_t, t)\|_2^2 \quad (1)$$

where $v_t(\mathbf{x}_t | \mathbf{x}_1)$ denotes the target conditional velocity. In Euclidean space, this target is typically induced by the linear interpolation between \mathbf{x}_0 and \mathbf{x}_1 , which yields a simple closed-form velocity field. Recent work extends the same principle to Riemannian manifolds [Chen and Lipman, 2023, Lipman et al., 2024], replacing Euclidean linear paths with geodesics and defining target velocities in the corresponding tangent spaces. Consistently, the geodesic degrades to the linear interpolation when the manifold is the Euclidean space, which means that the Riemannian flow matching is a strict generalization of the Euclidean case. These formulations show that flow matching is not restricted to flat Euclidean domains and provide the foundation for geometry-aware generative modeling.

3 Methodology

In this section, we present our proposed method, RMG.

Notation. Unless specified otherwise, \mathcal{M} denotes a Riemannian manifold. For $\mathbf{x} \in \mathcal{M}$, $T_{\mathbf{x}}\mathcal{M}$ denotes the tangent space at \mathbf{x} , and $T\mathcal{M}$ denotes the tangent bundle. We write $\text{Exp}_{\mathbf{x}} : T_{\mathbf{x}}\mathcal{M} \rightarrow \mathcal{M}$ and $\text{Log}_{\mathbf{x}} : \mathcal{M} \rightarrow T_{\mathbf{x}}\mathcal{M}$ for the exponential and logarithm maps, respectively. For embedded manifolds, $\Pi_{T_{\mathbf{x}}\mathcal{M}}(\cdot)$ denotes the projection operator onto $T_{\mathbf{x}}\mathcal{M}$.

3.1 Motion Representation and Manifold

Prior work typically factorizes a single motion frame into several parts as illustrated in Table 1. We adopt this decomposition but cast each factor on its natural Riemannian manifold, yielding a scale-free representation with intrinsic normalization. Unlike previous works that still apply dataset-level mean/standard-deviation normalization after forming the representation, the manifold structure (unit quaternions, pre-shapes, and a canonical length for translation) makes normalization unnecessary and enables geometry-aware modeling.

Global Translation (\mathcal{T}). Following common practice, we choose a specific joint of human body (usually chosen as the root joint, pelvis) to represent the global translation, which is a simple Euclidean space of \mathbb{R}^3 . This factor captures the global trajectory of the motion and is essential for modeling locomotion and spatial movement.

Global Orientation and Per-Joint Rotations (\mathcal{R}). The articulated rotations can be represented by unit quaternions. For a skeleton with J joints, we write $q = \{q_j\}_{j=1}^J$ with $q_j \in \mathbb{H}$ and $\|q_j\|_2 = 1$. Inspired by the SMPL parameterization [Loper et al., 2015], we define a canonical reference pose (typically the T-pose) and express all rotations relative to it: q_1 encodes the global orientation ($\mathcal{R}_{\text{Orientation}}$), while $\{q_j\}_{j=2}^J$ capture the local joint rotations in their respective local coordinate systems ($\mathcal{R}_{\text{Joint}}$). Since each q_j is a unit quaternion, it lies on the hypersphere \mathbb{S}^3 (embedded in \mathbb{R}^4), and the rotation component lies on the product manifold $(\mathbb{S}^3)^J$.

Unlike continuous 6D rotations [Zhou et al., 2019], unit quaternions represent $\text{SO}(3)$ without redundancy and induce smooth geodesics on \mathbb{S}^3 . This improves interpolation and sampling stability, avoids re-orthogonalization, and reduces dimensionality from 6 to 4 with a consistent distance metric.

Local Pose (\mathcal{P}). We represent the within-frame skeletal configuration as a point in the Kendall pre-shape space [Kendall, 1984, 1989, Dryden and Mardia, 2016]. Treating the J joints as landmarks in \mathbb{R}^3 , the pre-shape is invariant to global translation and scale and thus captures only the relative joint configuration within each frame. Concretely, \mathcal{S}_3^J denotes the set of centered configurations with unit Frobenius norm.

Given joint coordinates $P \in \mathbb{R}^{J \times 3}$, we remove global translation by centering and remove scale by Frobenius normalization:

$$p = \frac{P - \bar{P}}{\|P - \bar{P}\|_F} \in \mathcal{S}_3^J, \quad \bar{P} = \frac{1}{J} \sum_{j=1}^J P_j. \quad (2)$$

Unlike variants that only subtract the root (or XZ-plane) translation, this pre-shape is fully translation-invariant and scale-free, making it well-suited for modeling the local pose factor.

Temporal Differentiation (d.). For each factor, we can also include its temporal difference (e.g., velocity) as an additional component. Specifically, we can compute the temporal difference by $d\mathbf{x}_t = \text{Log}_{\mathbf{x}_t}(\mathbf{x}_{t+1}) \in T_{\mathbf{x}_t}\mathcal{M}_{\mathcal{F}}$ for $\mathcal{F} \in \{\mathcal{T}, \mathcal{R}, \mathcal{P}\}$. This captures the dynamic aspect of motion.

Unified View. Figure 2 illustrates our formulation, which provides us a unified view of motion representation as a product manifold of the composite factors and covers all the representation in the previous works. Take the HumanML3D [Guo et al., 2022] format without the foot contact indicator as an example, it corresponds to a product manifold of the form:

$$\mathcal{M}_{\text{H3D}} = T\mathcal{M}_{\mathcal{T}} \times T\mathcal{M}_{\mathcal{R}_{\text{Orientation}}} \times \mathcal{M}_{\mathcal{R}_{\text{Joint}}} \times \mathcal{M}_{\mathcal{P}} \times T\mathcal{M}_{\mathcal{P}}$$

However, using so many factors is redundant and not necessary. In this work, we argue global translation (\mathcal{T}), global orientation, and joint rotations (\mathcal{R}) are sufficient to capture articulated motion, which are verified through empirical studies (Section 4) and theoretical analysis (Section B). We therefore adopt a more compact representation that omits the pre-shape and other temporal differences, yielding

$$\mathcal{M}_{\text{RMG}} = \mathcal{M}_{\mathcal{T}} \times \mathcal{M}_{\mathcal{R}} = \mathbb{R}^3 \times (\mathbb{S}^3)^J, \quad (3)$$

We will elaborate and justify this choice in the ablation study (Section 4.3).

3.2 Prior Distribution

Riemannian Gaussian Distribution. We first introduce a mean-centered wrapped Gaussian distribution on a general Riemannian manifold \mathcal{M} . Given a reference (mean) point $\mu \in \mathcal{M}$, we draw Gaussian noise in its embedded Euclidean space \mathbb{R}^n , map it to the tangent space $T_{\mu}\mathcal{M}$ (via a projection operator), and then “wrap” it onto the manifold using the exponential map:

$$\xi \sim \mathcal{N}(0, \Sigma) \in \mathbb{R}^n, \quad v = \Pi_{T_{\mu}\mathcal{M}}(\xi) \in T_{\mu}\mathcal{M}, \quad z = \text{Exp}_{\mu}(v) \in \mathcal{M},$$

where Σ is typically chosen block-diagonal. Such distribution can be denoted as $\mathcal{RN}(\mu, \Sigma)$.

Choice of Reference Point. The reference point μ can be chosen arbitrarily, but a good choice improves sampling quality. For motion generation, we set μ to the *rest pose* with zero translation and identity rotations, which is a natural center of the motion manifold. This choice ensures that samples from the prior correspond to plausible static poses, providing a meaningful starting point for motion synthesis.

Specifically, for the translation factor, we set $\mu_{\mathcal{T}} = \mathbf{0} \in \mathbb{R}^3$; for the rotation factor, we set $\mu_{\mathcal{R}} = [1, 0, 0, 0] \in \mathbb{S}^3$; for the pre-shape factor (if used), we set $\mu_{\mathcal{P}}$ to the canonical T-pose after removing global translation and normalizing using Equation (2). In our chosen manifold \mathcal{M}_{RMG} (Equation (3)), the reference point is thus

$$\mu = (\underbrace{\mu_{\mathcal{T}}, \mu_{\mathcal{R}}, \mu_{\mathcal{R}}, \dots, \mu_{\mathcal{R}}}_{J \text{ times}}) \in \mathcal{M}_{\text{RMG}}.$$

3.3 Training and Inference

We train a time-dependent vector field on the motion manifold \mathcal{M} with Riemannian flow matching. Let $\mathbf{x}_1 \sim p_{\text{data}}$ denote a real motion sample and $\mathbf{x}_0 \sim p_0$ a prior sample (Section 3.2). For $t \sim \mathcal{U}[0, 1]$, we construct the interpolation state on the geodesic from \mathbf{x}_0 to \mathbf{x}_1 :

$$\mathbf{x}_t = \text{Exp}_{\mathbf{x}_0}(t \text{Log}_{\mathbf{x}_0}(\mathbf{x}_1)),$$

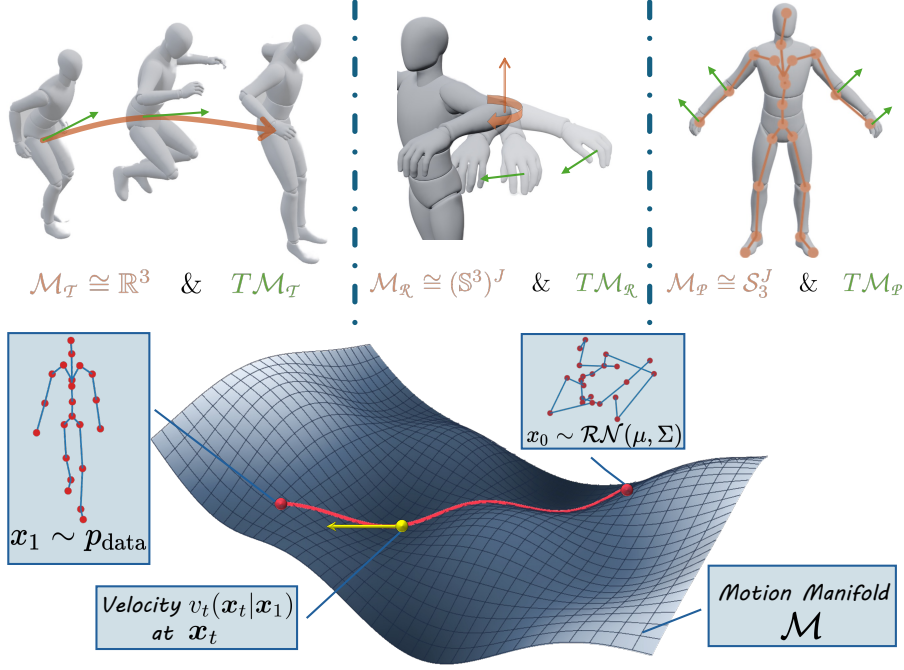


Figure 2: **(Top)** Illustration of the unified Riemannian representation for articulated motion. Each motion frame can be factorized into **global translation** ($\mathcal{M}_{\mathcal{T}}$), **global orientation and per-joint rotations** ($\mathcal{M}_{\mathcal{R}}$), and **local pose** ($\mathcal{M}_{\mathcal{P}}$) along with the **temporal differences** ($T\mathcal{M}_{\mathcal{F}}$ for $\mathcal{F} \in \{\mathcal{T}, \mathcal{R}, \mathcal{P}\}$). Each factor is represented on its natural Riemannian manifold, yielding a scale-free representation with intrinsic normalization. **(Bottom)** Illustration of the Riemannian flow matching process in the RMG manifold. \mathcal{M} is defined by our proposed manifold Equation (3). The red line is the geodesic between \mathbf{x}_0 and \mathbf{x}_1 while the yellow line with arrow is the velocity at \mathbf{x}_t .

On product manifolds, Exp and Log are applied factor-wise. The translation factor is Euclidean, while rotation and (optional) pre-shape factor use the corresponding manifold maps. The supervision signal is the geodesic tangent at \mathbf{x}_t , written as

$$v_t(\mathbf{x}_t | \mathbf{x}_1) = \frac{1}{1-t} \text{Log}_{\mathbf{x}_t}(\mathbf{x}_1) \in T_{\mathbf{x}_t}\mathcal{M},$$

which reduces to the standard Euclidean flow-matching target when $\mathcal{M} = \mathbb{R}^n$.

We parameterize the vector field by a neural network $v_{\theta}(\mathbf{x}_t, t)$. Since the output of the neural network is in the ambient Euclidean space, we must project it to the tangent space to enforce valid manifold dynamics: $\Pi_{T_{\mathbf{x}_t}\mathcal{M}}v_{\theta}(\mathbf{x}_t, t) \in T_{\mathbf{x}_t}\mathcal{M}$.

Training minimizes the mean-squared error between target and predicted tangent velocities:

$$\mathcal{L}(\theta) = \mathbb{E}_{\mathbf{x}_1 \sim p_{\text{data}}, \mathbf{x}_0 \sim p_0, t \sim \mathcal{U}[0,1]} \left[\left\| v_t(\mathbf{x}_t | \mathbf{x}_1) - \Pi_{T_{\mathbf{x}_t}\mathcal{M}}v_{\theta}(\mathbf{x}_t, t) \right\|_2^2 \right]. \quad (4)$$

At inference time, we sample $\mathbf{x}_0 \sim p_0$ and integrate the learned manifold ODE:

$$\frac{d\mathbf{x}_t}{dt} = \Pi_{T_{\mathbf{x}_t}\mathcal{M}}v_{\theta}(\mathbf{x}_t, t), \quad \mathbf{x}_0 \sim p_0, \quad (5)$$

from $t = 0$ to $t = 1$. With step size h , a first-order Riemannian Euler update is $\mathbf{x}_{t+h} = \text{Exp}_{\mathbf{x}_t}(h \Pi_{T_{\mathbf{x}_t}\mathcal{M}}v_{\theta}(\mathbf{x}_t, t))$, which preserves manifold constraints by construction.

We emphasize that $T\mathcal{M}_{\mathcal{F}}$, with $\mathcal{F} \in \{\mathcal{T}, \mathcal{R}, \mathcal{P}\}$, in Section 3.1 and $T_{\mathbf{x}_t}\mathcal{M}$ in Section 3.3 refer to different objects despite the similar notation. The former appears in the factorized motion representation and denotes optional temporal-difference components attached to data samples, which therefore belong to the data distribution $p_{\text{data}} = p_1$. The latter is the tangent space at the interpolation state \mathbf{x}_t and contains the time-dependent velocity field used by Riemannian flow matching, corresponding to the intermediate probability flow p_t .

4 Experiments

4.1 Experiment Setup

Datasets. The experiments are mainly conducted on *HumanML3D* [Guo et al., 2022]. HumanML3D is a large-scale language-motion dataset comprising 14,616 motions and 44,970 text descriptions building upon the AMASS dataset [Mahmood et al., 2019]. Besides HumanML3D, we also employ *MotionMillion* [Fan et al., 2025], which is a recently released large-scale motion dataset with 1 million motion clips and 4 million text descriptions, to pre-train our model and evaluate its generalization ability.

Evaluation Metrics. Following previous works [Guo et al., 2022, Chen et al., 2023, Tevet et al., 2022], we employ 4 main metrics to evaluate our framework. The Frechet Inception Distance is used to measure the motion quality as well as the feature distributions. The Diversity and MultiModality Distance are incorporated to measure the generation diversity. Lastly, the R Precision aims to evaluate the matching rate of the conditions.

Implementation Details. We use the Diffusion Transformer [Peebles and Xie, 2022] as the model backbone for the flow matching. For text encoding, we incorporate Qwen [Zhang et al., 2025, Yang et al., 2025], utilizing the encoded hidden states as the text representation. During training, we employ the AdamW [Loshchilov and Hutter, 2017] optimizer with a cosine learning-rate schedule and linear warmup: the learning rate is first warmed up linearly to 10^{-4} and then cosine-annealed to near zero. Training is performed in a classifier-free manner [Ho and Salimans, 2022] with a dropout rate of 10%. To stabilize both training and inference, we adopt an exponential moving average (EMA) strategy.

4.2 Main Results

Table 2: Evaluation of *text-based motion generation* on HumanML3D [Guo et al., 2022] dataset. Reported metrics are FID, R@1, Diversity, and MModality. The models in bold are the optimal models, and the models in underline are the sub-optimal models. The guidance scale is set to 6.5.

| Method | HumanML3D Format | | | | MotionStreamer Format | | | |
|-----------------------|------------------|--------------|--------------|--------------|-----------------------|--------------|---------------|---------------|
| | FID↓ | R@1↑ | Div→ | MModality↑ | FID↓ | R@1↑ | Div→ | MModality↑ |
| GT | 0.002 | 0.511 | 9.503 | 2.799 | 0.002 | 0.702 | 27.492 | – |
| MLD [2023] | 0.473 | 0.481 | 9.724 | 2.413 | 18.236 | 0.546 | 26.352 | – |
| T2M-GPT[2023] | 0.116 | 0.492 | 9.761 | 1.856 | 12.475 | 0.606 | 27.275 | – |
| MotionGPT [2023] | 0.232 | 0.492 | 9.528 | 2.008 | 14.375 | 0.456 | 27.114 | – |
| MoMask [2024] | <u>0.045</u> | 0.521 | – | 1.241 | 12.232 | 0.621 | 27.127 | – |
| MotionLCM [2024] | 0.304 | 0.505 | 9.607 | 2.259 | – | – | – | – |
| MotionCLR [2024] | 0.269 | 0.542 | 9.607 | 1.985 | – | – | – | – |
| MotionLab [2025] | 0.167 | – | 9.593 | 2.912 | – | – | – | – |
| MARDM [2025] | 0.114 | 0.500 | – | 2.231 | – | – | – | – |
| MotionStreamer [2025] | – | – | – | – | <u>11.790</u> | <u>0.631</u> | <u>27.284</u> | – |
| Ours | 0.043 | <u>0.525</u> | 9.555 | <u>2.748</u> | 5.835 | 0.710 | 27.672 | 14.906 |

We first evaluate our method on the HumanML3D text-to-motion generation benchmark and compare it with several strong baselines, including both diffusion-based methods (e.g., MotionDiffuse [Zhang et al., 2024], MDM [Tevet et al., 2022], MotionLab [Guo et al., 2025]) and autoregressive methods (e.g., T2M-GPT [Zhang et al., 2023], MGPT [Jiang et al., 2023], MoMask [Guo et al., 2024]). We report results under two output formats: the standard HumanML3D format and the MotionStreamer format. *It is worth noting that we implement extra functions to convert our Riemannian representation to either the HumanML3D format or MotionStreamer format for fair comparison. Refer to supplementary materials Section D.3 for details.*

Table 2 reports quantitative results of the 4 metrics on HumanML3D under two formats, where we focus primarily on the standard HumanML3D format. In this setting, our method achieves the best FID (0.043), slightly surpassing the previous best MoMask (0.045), indicating stronger motion realism and distribution matching. At the same time, our model maintains strong text-motion consistency with $R@1 = 0.525$ (second only to MotionCLR at 0.542), while preserving high generation diversity

and multimodality (Div = 9.555 and MModality = 2.748). Compared with prior methods that optimize only part of this trade-off (e.g., lower FID or higher R@1 alone), our model provides a more balanced improvement across quality, alignment, and diversity, which is critical for practical text-to-motion generation. For completeness, under the MotionStreamer format our method ranks first among all reported metrics (FID = 5.835, R@1 = 0.710, Div = 27.672, MModality = 14.906), further supporting the robustness of the learned Riemannian representation across output formats. We also provide additional results in the supplementary materials.

We further evaluate text-based motion generation on the large-scale MotionMillion benchmark to assess whether the advantages of our representation persist in a substantially broader data regime. Table 3 shows that our model (*Ours*, 0.5B+1.7B) outperforms the MotionMillion baselines across both fidelity and text alignment, while also exhibiting a clear and favorable guidance trade-off. With guidance scale 2.0, our method attains better FID of 5.6, improving substantially over the strongest baseline MotionMillion-7B (10.3) and thus reducing the distribution gap by nearly half. Increasing the guidance scale to 3.0 further raises R@1 from 0.81 to 0.86, while still maintaining a stronger FID than previous baselines. These results are particularly notable because our approach remains superior to substantially when scaling up, indicating that the gains come not merely from model scaling, but from the effectiveness of the proposed Riemannian motion representation and flow-matching formulation.

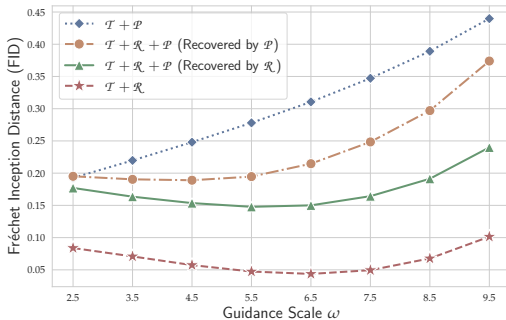
Overall, these findings highlight the scalability and generalization ability of our **RMG** framework, which can be effectively applied to both small and large datasets and models while maintaining superior performance across key metrics.

4.3 Ablation Studies

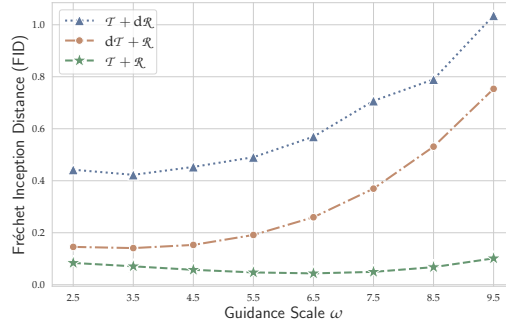
In this section, we conduct ablation studies to analyze the impact of different factors in our framework, and we answer two main research questions:

RQ1: Which factors matter for motion quality and guidance stability?

RQ2: Does temporal difference modeling improve motion quality?



(a) We study the impact of the Riemannian representation including $\mathcal{T} + \mathcal{R}$, $\mathcal{T} + \mathcal{R} + \mathcal{P}$ and $\mathcal{T} + \mathcal{P}$.



(b) We study the impact of temporal difference modeling in our framework including $\mathcal{T} + \mathcal{R}$, $d\mathcal{T} + \mathcal{R}$, $\mathcal{T} + d\mathcal{R}$.

Figure 3: Ablation study on different factors of our framework. All the models are trained with the same setting (including the parameter size, random seed) and evaluated on the HumanML3D benchmark.

Table 3: Evaluation of *text-based motion generation* on MotionMillion [Fan et al., 2025] dataset. Reported metrics are FID and R@1. In our method, 0.5B and 1.7B refer to the parameter sizes of our Riemannian flow matching model and Qwen3-1.7B, respectively. G.S. refers to the guidance scale.

| Method | G.S. | FID↓ | R@1↑ |
|------------------|------|------------|-------------|
| ScaMo [2025] | – | 89.0 | 0.67 |
| MotionMillion-3B | – | 10.8 | 0.79 |
| MotionMillion-7B | – | 10.3 | 0.79 |
| Ours (0.5B+1.7B) | 2.0 | 5.6 | <u>0.81</u> |
| Ours (0.5B+1.7B) | 3.0 | <u>7.8</u> | 0.86 |

RQ1. To isolate the role of each factor, we keep the same architecture and training setup and only change the representation, then sweep the guidance scale $\omega \in [2.5, 9.5]$. Figure 3a shows that $\mathcal{T} + \mathcal{R}$ is consistently the best and most stable setting: its FID decreases from approximately 0.084 ($\omega = 2.5$) to a minimum of about 0.043 ($\omega = 6.5$), and remains low even at large guidance (0.101 at $\omega = 9.5$). In contrast, $\mathcal{T} + \mathcal{P}$ degrades monotonically as guidance increases (from 0.20 to 0.44), indicating poor robustness without rotation information.

For $\mathcal{T} + \mathcal{R} + \mathcal{P}$, the term ‘Recovered by \cdot ’ means different conversion functions used to convert to the HumanML3D format for evaluation. Refer to Section D.3 for details. We find that recovering with \mathcal{R} is consistently better than recovering with \mathcal{P} across the entire guidance range (e.g., 0.043 vs. 0.084 at $\omega = 2.5$, and 0.101 vs. 0.44 at $\omega = 9.5$). This suggests that the rotation component is more critical for maintaining motion quality and stability under guidance, while the pose-coordinate component does not provide additional robustness in this setup.

This trend is also aligned with practical motion representations: in real animation and robotics pipelines, motion is predominantly driven by global/root translation and joint rotations. By contrast, pose-coordinate representations are more affected by subject-specific factors (e.g., body scale and limb proportions), which introduces additional variability across people. Taken together, these observations suggest that $\mathcal{T} + \mathcal{R}$ is a compact and robust representation that is sufficient for motion modeling in our setting.

RQ2. To answer whether temporal difference modeling improves motion quality, we compare $\mathcal{T} + \mathcal{R}$ with $d\mathcal{T} + \mathcal{R}$ and $\mathcal{T} + d\mathcal{R}$ under the same guidance sweep $\omega \in [2.5, 9.5]$. Figure 3b shows that $\mathcal{T} + \mathcal{R}$ consistently attains the lowest FID across the full range of ω . In contrast, $d\mathcal{T} + \mathcal{R}$ degrades steadily as guidance increases (0.14 \rightarrow 0.75), and $\mathcal{T} + d\mathcal{R}$ is less stable still (0.44 \rightarrow 1.03). This behavior is consistent with the representation property of temporal differencing: it attenuates absolute/global motion state (e.g., global trajectory and orientation) while emphasizing local frame-to-frame variation, which weakens long-horizon structure modeling. Overall, temporal differencing does not improve performance in our setting, and absolute modeling of translation and rotation ($\mathcal{T} + \mathcal{R}$) remains the most robust choice for guidance-stable generation.

5 Conclusion

Limitations. Though our work has demonstrated promising results, there are certain limitations including lack of further exploration of more condition modalities and the potential for facial and hand motion modeling. We leave more discussion in the supplementary materials Section E.

In conclusion, we proposed **Riemannian Motion Generation (RMG)**, a unified geometric framework for human motion representation and generation. Instead of treating motion as an unconstrained Euclidean vector, we modeled it on a product manifold and learned generation dynamics with Riemannian flow matching. This design yields a compact representation, $\mathbb{R}^3 \times (\mathbb{S}^3)^J$, together with a geometry-consistent training and inference pipeline based on geodesic interpolation, tangent-space vector-field learning, and manifold-preserving integration.

Extensive experiments demonstrated that this geometric formulation is both effective and scalable. RMG achieves strong and balanced performance on HumanML3D across motion quality, text alignment, and diversity, and generalizes well to the larger MotionMillion benchmark. Our ablation studies further showed that translation and rotation factors are sufficient in practice, while adding extra factors does not necessarily improve generation quality. Overall, the results support representation geometry as a core design principle for motion generation.

References

- Michael S Albergo, Nicholas M Boffi, and Eric Vanden-Eijnden. Stochastic interpolants: A unifying framework for flows and diffusions. *arXiv preprint arXiv:2303.08797*, 2023.
- Tenglong Ao, Qingzhe Gao, Yuke Lou, Baoquan Chen, and Libin Liu. Rhythmic gesticulator: Rhythm-aware co-speech gesture synthesis with hierarchical neural embeddings. *ACM Transactions on Graphics (TOG)*, 41(6):1–19, 2022.

- Huanqia Cai, Sihan Cao, Ruoyi Du, Peng Gao, Steven Hoi, Zhaohui Hou, Shijie Huang, Dengyang Jiang, Xin Jin, Liangchen Li, et al. Z-image: An efficient image generation foundation model with single-stream diffusion transformer. *arXiv preprint arXiv:2511.22699*, 2025.
- Kang Chen, Zhipeng Tan, Jin Lei, Song-Hai Zhang, Yuan-Chen Guo, Weidong Zhang, and Shi-Min Hu. Choreomaster: choreography-oriented music-driven dance synthesis. *ACM Transactions on Graphics (TOG)*, 40(4):1–13, 2021.
- Ling-Hao Chen, Shunlin Lu, Wenxun Dai, Zhiyang Dou, Xuan Ju, Jingbo Wang, Taku Komura, and Lei Zhang. Pay attention and move better: Harnessing attention for interactive motion generation and training-free editing. *arXiv preprint arXiv:2410.18977*, 2024.
- Ricky TQ Chen and Yaron Lipman. Flow matching on general geometries. *arXiv preprint arXiv:2302.03660*, 2023.
- Xin Chen, Biao Jiang, Wen Liu, Zilong Huang, Bin Fu, Tao Chen, and Gang Yu. Executing your commands via motion diffusion in latent space. In *Proceedings of the IEEE/CVF conference on computer vision and pattern recognition*, pages 18000–18010, 2023.
- Rishabh Dabral, Muhammad Hamza Mughal, Vladislav Golyanik, and Christian Theobalt. Mofusion: A framework for denoising-diffusion-based motion synthesis. In *Proceedings of the IEEE/CVF conference on computer vision and pattern recognition*, pages 9760–9770, 2023.
- Wenxun Dai, Ling-Hao Chen, Jingbo Wang, Jinpeng Liu, Bo Dai, and Yansong Tang. Motionlcm: Real-time controllable motion generation via latent consistency model. In *European Conference on Computer Vision*, pages 390–408. Springer, 2024.
- Bruno Degardin, Joao Neves, Vasco Lopes, Joao Brito, Ehsan Yaghoubi, and Hugo Proença. Generative adversarial graph convolutional networks for human action synthesis. In *Proceedings of the IEEE/CVF Winter Conference on Applications of Computer Vision*, pages 1150–1159, 2022.
- Ian L. Dryden and Kanti V. Mardia. *Statistical Shape Analysis, with Applications in R*. Wiley, 2 edition, 2016.
- Patrick Esser, Sumith Kulal, Andreas Blattmann, Rahim Entezari, Jonas Müller, Harry Saini, Yam Levi, Dominik Lorenz, Axel Sauer, Frederic Boesel, et al. Scaling rectified flow transformers for high-resolution image synthesis. In *Forty-first international conference on machine learning*, 2024.
- Ke Fan, Shunlin Lu, Minyue Dai, Runyi Yu, Lixing Xiao, Zhiyang Dou, Junting Dong, Lizhuang Ma, and Jingbo Wang. Go to zero: Towards zero-shot motion generation with million-scale data. In *Proceedings of the IEEE/CVF International Conference on Computer Vision*, pages 13336–13348, 2025.
- Ian J Goodfellow, Jean Pouget-Abadie, Mehdi Mirza, Bing Xu, David Warde-Farley, Sherjil Ozair, Aaron Courville, and Yoshua Bengio. Generative adversarial nets. *Advances in neural information processing systems*, 27, 2014.
- Chuan Guo, Xinxin Zuo, Sen Wang, Shihao Zou, Qingyao Sun, Annan Deng, Minglun Gong, and Li Cheng. Action2motion: Conditioned generation of 3d human motions. In *Proceedings of the 28th ACM International Conference on Multimedia*, pages 2021–2029, 2020.
- Chuan Guo, Shihao Zou, Xinxin Zuo, Sen Wang, Wei Ji, Xingyu Li, and Li Cheng. Generating diverse and natural 3d human motions from text. In *Proceedings of the IEEE/CVF conference on computer vision and pattern recognition*, pages 5152–5161, 2022.
- Chuan Guo, Yuxuan Mu, Muhammad Gohar Javed, Sen Wang, and Li Cheng. Momask: Generative masked modeling of 3d human motions. In *Proceedings of the IEEE/CVF Conference on Computer Vision and Pattern Recognition*, pages 1900–1910, 2024.
- Ziyan Guo, Zeyu Hu, De Wen Soh, and Na Zhao. Motionlab: Unified human motion generation and editing via the motion-condition-motion paradigm. In *Proceedings of the IEEE/CVF International Conference on Computer Vision*, pages 13869–13879, 2025.
- Jonathan Ho and Tim Salimans. Classifier-free diffusion guidance. *arXiv preprint arXiv:2207.12598*, 2022.
- Ruozi Huang, Huang Hu, Wei Wu, Kei Sawada, Mi Zhang, and Daxin Jiang. Dance revolution: Long-term dance generation with music via curriculum learning. In *International conference on learning representations*, 2020.
- Biao Jiang, Xin Chen, Wen Liu, Jingyi Yu, Gang Yu, and Tao Chen. Motiongpt: Human motion as a foreign language. *Advances in Neural Information Processing Systems*, 36:20067–20079, 2023.

- David G. Kendall. Shape manifolds, procrustean metrics, and complex projective spaces. *Bulletin of the London Mathematical Society*, 16(2):81–121, 1984.
- David G Kendall. A survey of the statistical theory of shape. *Statistical Science*, 4(2):87–99, 1989.
- Jihoon Kim, Jiseob Kim, and Sungjoon Choi. Flame: Free-form language-based motion synthesis & editing. In *Proceedings of the AAAI Conference on Artificial Intelligence*, volume 37, pages 8255–8263, 2023.
- Jinwoo Kim, Heeseok Oh, Seongjean Kim, Hoseok Tong, and Sanghoon Lee. A brand new dance partner: Music-conditioned pluralistic dancing controlled by multiple dance genres. In *Proceedings of the IEEE/CVF Conference on Computer Vision and Pattern Recognition*, pages 3490–3500, 2022.
- Diederik P Kingma, Max Welling, et al. Auto-encoding variational bayes, 2013.
- John M. Lee. *Introduction to Smooth Manifolds*. Springer, 2 edition, 2012.
- John M. Lee. *Introduction to Riemannian Manifolds*. Springer, 2 edition, 2018.
- Ruilong Li, Shan Yang, David A Ross, and Angjoo Kanazawa. Ai choreographer: Music conditioned 3d dance generation with aist++. In *Proceedings of the IEEE/CVF international conference on computer vision*, pages 13401–13412, 2021.
- Yaron Lipman, Ricky TQ Chen, Heli Ben-Hamu, Maximilian Nickel, and Matt Le. Flow matching for generative modeling. *arXiv preprint arXiv:2210.02747*, 2022.
- Yaron Lipman, Marton Havasi, Peter Holderrieth, Neta Shaul, Matt Le, Brian Karrer, Ricky TQ Chen, David Lopez-Paz, Heli Ben-Hamu, and Itai Gat. Flow matching guide and code. *arXiv preprint arXiv:2412.06264*, 2024.
- Haiyang Liu, Naoya Iwamoto, Zihao Zhu, Zhengqing Li, You Zhou, Elif Bozkurt, and Bo Zheng. Disco: Disentangled implicit content and rhythm learning for diverse co-speech gestures synthesis. In *Proceedings of the 30th ACM international conference on multimedia*, pages 3764–3773, 2022a.
- Xingchao Liu, Chengyue Gong, and Qiang Liu. Flow straight and fast: Learning to generate and transfer data with rectified flow. *arXiv preprint arXiv:2209.03003*, 2022b.
- Matthew Loper, Naureen Mahmood, Javier Romero, Gerard Pons-Moll, and Michael J. Black. SMPL: A skinned multi-person linear model. *ACM Trans. Graphics (Proc. SIGGRAPH Asia)*, 34(6):248:1–248:16, October 2015.
- Ilya Loshchilov and Frank Hutter. Decoupled weight decay regularization. *arXiv preprint arXiv:1711.05101*, 2017.
- Shunlin Lu, Jingbo Wang, Zeyu Lu, Ling-Hao Chen, Wenxun Dai, Junting Dong, Zhiyang Dou, Bo Dai, and Ruimao Zhang. Scamo: Exploring the scaling law in autoregressive motion generation model. In *Proceedings of the Computer Vision and Pattern Recognition Conference*, pages 27872–27882, 2025.
- Naureen Mahmood, Nima Ghorbani, Nikolaus F. Troje, Gerard Pons-Moll, and Michael J. Black. AMASS: Archive of motion capture as surface shapes. In *International Conference on Computer Vision*, pages 5442–5451, October 2019.
- Zichong Meng, Yiming Xie, Xiaogang Peng, Zeyu Han, and Huaizu Jiang. Rethinking diffusion for text-driven human motion generation: Redundant representations, evaluation, and masked autoregression. In *Proceedings of the Computer Vision and Pattern Recognition Conference*, pages 27859–27871, 2025.
- William S Peebles and Saining Xie. Scalable diffusion models with transformers. 2023 ieee. In *CVF International Conference on Computer Vision (ICCV)*, volume 4172, 2022.
- Xavier Pennec. Intrinsic statistics on riemannian manifolds: Basic tools for geometric measurements. *Journal of Mathematical Imaging and Vision*, 25(1):127–154, 2006.
- Mathis Petrovich, Michael J Black, and Gül Varol. Action-conditioned 3d human motion synthesis with transformer vae. In *Proceedings of the IEEE/CVF International Conference on Computer Vision*, pages 10985–10995, 2021.
- Mathis Petrovich, Michael J Black, and Gül Varol. Temos: Generating diverse human motions from textual descriptions. In *European Conference on Computer Vision*, pages 480–497. Springer, 2022.
- Danilo Rezende and Shakir Mohamed. Variational inference with normalizing flows. In *International conference on machine learning*, pages 1530–1538. PMLR, 2015.

- Salem Said, Lionel Bombrun, Yannick Berthoumieu, and Jonathan H. Manton. Riemannian gaussian distributions on the space of symmetric positive definite matrices. *IEEE Transactions on Information Theory*, 63(4):2153–2170, 2017.
- Guy Tevet, Sigal Raab, Brian Gordon, Yonatan Shafir, Daniel Cohen-Or, and Amit H Bermano. Human motion diffusion model. *arXiv preprint arXiv:2209.14916*, 2022.
- Jonathan Tseng, Rodrigo Castellon, and Karen Liu. Edge: Editable dance generation from music. In *Proceedings of the IEEE/CVF Conference on Computer Vision and Pattern Recognition*, pages 448–458, 2023.
- Guillermo Valle-Pérez, Gustav Eje Henter, Jonas Beskow, Andre Holzapfel, Pierre-Yves Oudeyer, and Simon Alexanderson. Transflower: probabilistic autoregressive dance generation with multimodal attention. *ACM Transactions on Graphics (TOG)*, 40(6):1–14, 2021.
- Lixing Xiao, Shunlin Lu, Huaijin Pi, Ke Fan, Liang Pan, Yueer Zhou, Ziyong Feng, Xiaowei Zhou, Sida Peng, and Jingbo Wang. Motionstreamer: Streaming motion generation via diffusion-based autoregressive model in causal latent space. In *Proceedings of the IEEE/CVF International Conference on Computer Vision*, pages 10086–10096, 2025.
- An Yang, Anfeng Li, Baosong Yang, Beichen Zhang, Binyuan Hui, Bo Zheng, Bowen Yu, Chang Gao, Chengen Huang, Chenxu Lv, et al. Qwen3 technical report. *arXiv preprint arXiv:2505.09388*, 2025.
- Ping Yu, Yang Zhao, Chunyuan Li, Junsong Yuan, and Changyou Chen. Structure-aware human-action generation. In *Computer Vision—ECCV 2020: 16th European Conference, Glasgow, UK, August 23–28, 2020, Proceedings, Part XXX 16*, pages 18–34. Springer, 2020.
- Jianrong Zhang, Yangsong Zhang, Xiaodong Cun, Yong Zhang, Hongwei Zhao, Hongtao Lu, Xi Shen, and Ying Shan. Generating human motion from textual descriptions with discrete representations. In *Proceedings of the IEEE/CVF conference on computer vision and pattern recognition*, pages 14730–14740, 2023.
- Mingyuan Zhang, Zhongang Cai, Liang Pan, Fangzhou Hong, Xinying Guo, Lei Yang, and Ziwei Liu. Motion-diffuse: Text-driven human motion generation with diffusion model. *IEEE transactions on pattern analysis and machine intelligence*, 46(6):4115–4128, 2024.
- Yanzhao Zhang, Mingxin Li, Dingkun Long, Xin Zhang, Huan Lin, Baosong Yang, Pengjun Xie, An Yang, Dayiheng Liu, Junyang Lin, Fei Huang, and Jingren Zhou. Qwen3 embedding: Advancing text embedding and reranking through foundation models. *arXiv preprint arXiv:2506.05176*, 2025.
- Yi Zhou, Connelly Barnes, Jingwan Lu, Jimei Yang, and Hao Li. On the continuity of rotation representations in neural networks. In *Proceedings of the IEEE/CVF conference on computer vision and pattern recognition*, pages 5745–5753, 2019.
- Wentao Zhu, Xiaoxuan Ma, Dongwoo Ro, Hai Ci, Jinlu Zhang, Jiabin Shi, Feng Gao, Qi Tian, and Yizhou Wang. Human Motion Generation: A Survey . *IEEE Transactions on Pattern Analysis & Machine Intelligence*, 46(04):2430–2449, April 2024. ISSN 1939-3539. doi: 10.1109/TPAMI.2023.3330935. URL <https://doi.ieeecomputersociety.org/10.1109/TPAMI.2023.3330935>.

Appendix

A Manifold

In this paper, we focus on three types of Riemannian manifolds: Euclidean space \mathbb{R}^3 , the hypersphere \mathbb{S}^3 , and the pre-shape space \mathcal{S}_3^J .

Euclidean space. Euclidean space \mathbb{R}^3 is a flat manifold with zero curvature. It is the most familiar manifold, where the distance between two points is simply their straight-line distance. Most existing diffusion models are built in this space.

Hypersphere. The hypersphere \mathbb{S}^3 is a curved manifold with constant positive curvature. It is embedded in \mathbb{R}^4 and consists of points at a fixed distance from the origin. In this work, we use the hypersphere to model quaternions. Since q and $-q$ represent the same rotation, we restrict quaternions to the upper hemisphere of \mathbb{S}^3 to avoid ambiguity during dataset construction. In other words, for any point $q = (w, x, y, z) \in \mathbb{S}^3$, we have $q_0 > 0$.

For Riemannian flow matching on a general hyper-sphere \mathcal{S}^d , consider two points $\mathbf{x}_0, \mathbf{x}_1 \in \mathbb{R}^{d+1}$ on the hypersphere \mathcal{S}^d . The geodesic between them can be written as

$$\gamma(t) = \frac{\sin((1-t)\theta)}{\sin(\theta)} \mathbf{x}_0 + \frac{\sin(t\theta)}{\sin(\theta)} \mathbf{x}_1,$$

where $\theta = \arccos(\langle \mathbf{x}_0, \mathbf{x}_1 \rangle)$ is the angle between \mathbf{x}_0 and \mathbf{x}_1 . The geodesic velocity at time t is given by:

$$\dot{\gamma}(t) = \frac{\theta}{\sin(\theta)} (-\sin(t\theta)\mathbf{x}_0 + \sin((1-t)\theta)\mathbf{x}_1).$$

Pre-shape space. The pre-shape space models the relative configuration of points. For example, the set of all triangles in \mathbb{R}^2 forms a pre-shape space, denoted by \mathcal{S}_2^3 . In this work, we use the pre-shape space \mathcal{S}_3^J to model the human skeleton, which consists of J joints in \mathbb{R}^3 . A pre-shape is represented by a $J \times 3$ matrix, where each row gives the coordinates of one joint. The pre-shape space is defined as the set of all such matrices that are centered at the centroid and normalized to unit Frobenius norm. A concrete formulation is given in Equation (2). Intrinsically, the pre-shape space can be viewed as a high-dimensional hypersphere, so geodesics can be computed in the same way as on the hypersphere.

Beyond the pre-shape space, one can also consider the shape space, which is the quotient of the pre-shape space by the rotation group: $\mathcal{S}_3^J \backslash \text{SO}(3)$. However, geodesic computation in the shape space is substantially more involved, so we only study the pre-shape space in this work.

For Riemannian flow matching on a general pre-shape space \mathcal{S}_m^k , for any two pre-shapes $\mathbf{X}_0, \mathbf{X}_1 \in \mathcal{S}_m^k$, define

$$\theta = \arccos \text{trace}(\mathbf{X}_0^\top \mathbf{X}_1), \quad 0 \leq \theta \leq \pi.$$

If $\mathbf{X}_0 \neq \pm \mathbf{X}_1$, the unique minimizing geodesic connecting \mathbf{X}_0 and \mathbf{X}_1 on \mathcal{S}_m^k is given by

$$\Gamma(t) = \frac{\sin((1-t)\theta)}{\sin \theta} \mathbf{X}_0 + \frac{\sin(t\theta)}{\sin \theta} \mathbf{X}_1, \quad t \in [0, 1].$$

and the geodesic velocity at time t is given by

$$\dot{\Gamma}(t) = \frac{\theta}{\sin \theta} (-\sin(t\theta)\mathbf{X}_0 + \sin((1-t)\theta)\mathbf{X}_1).$$

B Theoretical Support

B.1 Redundancy induces flat directions

Proposition 1 (Redundancy induces flat directions). *Let \mathcal{M} be a smooth m -dimensional manifold and let $\pi : U \subset \mathbb{R}^d \rightarrow \mathcal{M}$ be a smooth submersion with $d > m$. For any loss $L(z) = \ell(\pi(z))$, the gradient $\nabla L(z)$ is orthogonal to $\ker(D\pi(z))$, and the Hessian $\nabla^2 L(z)$ has at least $d - m$ zero eigenvalues at any critical point. In other words, representing an m -dimensional quantity in \mathbb{R}^d introduces $d - m$ flat directions in the loss landscape.*

Proof. Gradient claim. By the chain rule, the differential of L at z satisfies

$$dL_z = d\ell_{\pi(z)} \circ D\pi(z).$$

For any $v \in \ker(D\pi(z))$, we have $D\pi(z)v = 0$, so

$$\nabla L(z)^\top v = dL_z(v) = d\ell_{\pi(z)}(D\pi(z)v) = d\ell_{\pi(z)}(0) = 0.$$

Hence $\nabla L(z)$ is orthogonal to every redundant direction.

Hessian claim. Consider the curve $z(t) = z + tv$ and set $x(t) = \pi(z(t))$. Differentiating at $t = 0$ gives $x'(0) = D\pi(z)v = 0$. Differentiating $L(z(t)) = \ell(x(t))$ twice and evaluating at $t = 0$ yields

$$v^\top \nabla^2 L(z) v = \left. \frac{d^2}{dt^2} L(z(t)) \right|_{t=0} = \nabla \ell(x(0))^\top x''(0) + x'(0)^\top \nabla^2 \ell(x(0)) x'(0).$$

The second term vanishes because $x'(0) = 0$. At a critical point of L , the gradient claim above gives $\nabla L(z) = 0$, which by the chain rule forces $\nabla \ell(\pi(z)) = 0$, so the first term also vanishes. Therefore $v^\top \nabla^2 L(z) v = 0$ for all $v \in \ker(D\pi(z))$.

Zero eigenvalue count. Since π is a submersion, $\text{rank } D\pi(z) = m$, and rank-nullity gives $\dim \ker(D\pi(z)) = d - m$. The Hessian $\nabla^2 L(z)$ is symmetric, and every vector in this $(d - m)$ -dimensional subspace is a zero eigenvector, so $\nabla^2 L(z)$ has at least $d - m$ zero eigenvalues. \square

This proposition shows that when a representation contains redundant coordinates, the loss landscape contains intrinsically flat directions. These directions correspond to variations that do not change the underlying state on the manifold, which may lead to an ill-posed optimization problem and unstable training dynamics. On the contrast, a compact representation aligned with the intrinsic manifold removes these redundant degrees of freedom.

B.2 Statistical advantage of Riemannian Flow Matching

Proposition 2 (Informal statistical advantage of Riemannian Flow Matching). *Let (\mathcal{M}, g) be a compact d -dimensional Riemannian manifold embedded in \mathbb{R}^D with $d < D$, and suppose the data distribution is supported on \mathcal{M} . Let $X_t \in \mathcal{M}$ be a conditional interpolation, and let*

$$\rho_t := \text{Law}(X_t) \in \mathcal{P}(\mathcal{M})$$

denote its marginal distribution at time t . Define the target data distribution by

$$\rho_{\text{data}} := \rho_1.$$

Assume $\dot{X}_t \in T_{X_t} \mathcal{M}$, and define the conditional flow matching target by

$$u_t^*(x) = \mathbb{E}[\dot{X}_t \mid X_t = x].$$

Assume further that u^* belongs to an s -smooth class of tangent vector fields on \mathcal{M} . Then the Riemannian flow matching estimator \hat{u} satisfies

$$\mathbb{E} \left[\int_0^1 \|\hat{u}_t - u_t^*\|_{L^2(\rho_t; T\mathcal{M})}^2 dt \right] \lesssim n^{-\frac{2s}{2s+d}}.$$

Moreover, if $\hat{\rho}_{\text{data}}$ denotes the generated distribution at terminal time $t = 1$, then under standard flow stability assumptions,

$$\mathbb{E} W_2^2(\hat{\rho}_{\text{data}}, \rho_{\text{data}}) \lesssim n^{-\frac{2s}{2s+d}}.$$

By contrast, for Euclidean Flow Matching in the ambient space \mathbb{R}^D , one typically obtains

$$\mathbb{E} W_2^2(\hat{\rho}_{\text{data}}^{\text{EFM}}, \rho_{\text{data}}) \lesssim n^{-\frac{2s}{2s+D}}.$$

Since $d < D$, we have

$$n^{-\frac{2s}{2s+d}} \gg n^{-\frac{2s}{2s+D}},$$

and therefore the error bound of Riemannian Flow Matching is asymptotically strictly better than that of Euclidean Flow Matching.

Proof sketch. The flow matching population loss is

$$\mathcal{L}(u) = \mathbb{E}[\|u_t(X_t) - \dot{X}_t\|_g^2].$$

By the usual regression identity,

$$\mathcal{L}(u) - \mathcal{L}(u^*) = \int_0^1 \|u_t - u_t^*\|_{L^2(\rho_t; T\mathcal{M})}^2 dt.$$

Therefore, estimating the flow matching vector field reduces to a nonparametric regression problem on the intrinsic state space where the samples live.

If the model is formulated intrinsically on \mathcal{M} , then the relevant function class is an s -smooth class on a d -dimensional manifold. Standard entropy bounds on manifolds imply that its statistical complexity depends on the intrinsic dimension d , which yields the rate

$$n^{-\frac{2s}{2s+d}}.$$

In contrast, a naive Euclidean formulation in \mathbb{R}^D uses a D -dimensional ambient smooth class, leading to the slower rate

$$n^{-\frac{2s}{2s+D}}.$$

Finally, the terminal generated distribution is obtained by pushing the reference distribution through the learned flow up to time $t = 1$. Standard stability of the flow map implies that the error in the learned vector field controls the terminal distribution error, hence

$$\mathbb{E} W_2^2(\hat{\rho}_{\text{data}}, \rho_{\text{data}}) \lesssim n^{-\frac{2s}{2s+d}}.$$

Combining the two bounds and using $d < D$ shows that Riemannian Flow Matching has a strictly sharper asymptotic error estimate than Euclidean Flow Matching. \square

This proposition provides a theoretical justification for the statistical superiority of Riemannian Flow Matching over Euclidean Flow Matching when the data distribution is supported on a low-dimensional manifold embedded in a high-dimensional ambient space. When the data distribution lies on a d -dimensional manifold, learning flow matching in a manifold representation reduces the effective dimension of the regression problem for the velocity field. As a consequence, the Wasserstein error of the learned generative distribution scales with d rather than the ambient dimension D , leading to improved asymptotic rates.

C Additional Experiment Results

C.1 Full Results

Table 4: Full results on the HumanML3D dataset in H3D format.

| Method | HumanML3D Format | | | | | | |
|-------------|-------------------------------|-------------------------------|------------------------|------------------------|------------------------|-------------------------------|-------------------------------|
| | FID↓ | R@1↑ | R@2↑ | R@3↑ | MM-Dist↓ | Div→ | MM↑ |
| GT | 0.002 | 0.511 | 0.703 | 0.797 | 2.974 | 9.503 | 2.799 |
| MLD | 0.473 | 0.481 | 0.673 | 0.772 | 3.196 | 9.724 | 2.413 |
| T2M-GPT | 0.116 | 0.492 | 0.679 | 0.775 | 3.121 | 9.761 | 1.856 |
| MotionGPT | 0.232 | 0.492 | 0.681 | 0.733 | 3.096 | 9.528 | 2.008 |
| MoMask | <u>0.045</u> | 0.521 | <u>0.713</u> | 0.807 | 2.958 | – | 1.241 |
| MotionGPT-2 | 0.191 | 0.496 | 0.691 | 0.782 | 3.080 | 9.860 | 2.137 |
| MotionLCM | 0.304 | 0.505 | 0.705 | 0.805 | 2.986 | 9.607 | 2.259 |
| MotionCLR | 0.269 | 0.544 | 0.732 | 0.831 | 2.806 | 9.607 | 1.985 |
| MotionLab | 0.167 | – | – | <u>0.810</u> | <u>2.830</u> | 9.593 | 2.912 |
| MARDM | 0.114 | 0.500 | 0.695 | 0.795 | – | – | 2.231 |
| Ours | 0.043 ^{±.002} | <u>0.525</u> ^{±.002} | 0.711 ^{±.002} | 0.805 ^{±.002} | 2.930 ^{±.007} | <u>9.555</u> ^{±.060} | <u>2.748</u> ^{±.023} |

We report the full results of our method and all baselines on HumanML3D in both the original H3D format (Table 4) and the MotionStreamer format (Table 5), together with the full results on MotionMillion (Table 6). For HumanML3D, each experiment is repeated over 20 independent runs, and we report the mean with 95% confidence intervals computed using the t -distribution. For MotionMillion, the dataset scale and our compute budget limit evaluation to a single run.

Table 5: Full results on the HumanML3D dataset in MotionStreamer format.

| Method | MotionStreamer Format | | | | | | |
|----------------|-------------------------|-------------------------|-------------------------|-------------------------|--------------------------|--------------------------|--------------------------|
| | FID↓ | R@1↑ | R@2↑ | R@3↑ | MM-Dist↓ | Div→ | MM↑ |
| GT | 0.002 | 0.702 | 0.864 | 0.914 | 15.151 | 27.492 | – |
| MLD | 18.236 | 0.546 | 0.730 | 0.792 | 16.638 | 26.352 | – |
| T2M-GPT | 12.475 | 0.606 | 0.774 | 0.838 | 16.812 | 27.275 | – |
| MotionGPT | 14.375 | 0.456 | 0.598 | 0.628 | 17.892 | 27.114 | – |
| MoMask | 12.232 | 0.621 | 0.784 | 0.846 | 16.138 | 27.127 | – |
| MotionStreamer | <u>11.790</u> | <u>0.631</u> | <u>0.802</u> | <u>0.859</u> | <u>16.081</u> | <u>27.284</u> | – |
| Ours | 5.835 \pm .060 | 0.710 \pm .002 | 0.850 \pm .002 | 0.899 \pm .001 | 15.683 \pm .022 | 27.672 \pm .076 | 14.906 \pm .208 |

Table 6: Full results of MotionMillion dataset.

| Method | Guidance Scale | FID↓ | R@1↑ | R@2↑ | R@3↑ |
|------------------|----------------|-------------|-------------|-------------|-------------|
| ScaMo | – | 89.0 | 0.67 | 0.81 | 0.87 |
| MotionMillion-3B | – | 10.8 | 0.79 | 0.91 | 0.94 |
| MotionMillion-7B | – | <u>10.3</u> | <u>0.79</u> | 0.90 | 0.94 |
| Ours (0.5B+1.7B) | 2.0 | 5.6 | <u>0.81</u> | <u>0.92</u> | <u>0.95</u> |
| Ours (0.5B+1.7B) | 3.0 | <u>7.8</u> | 0.86 | 0.95 | 0.97 |

C.2 Training Stability

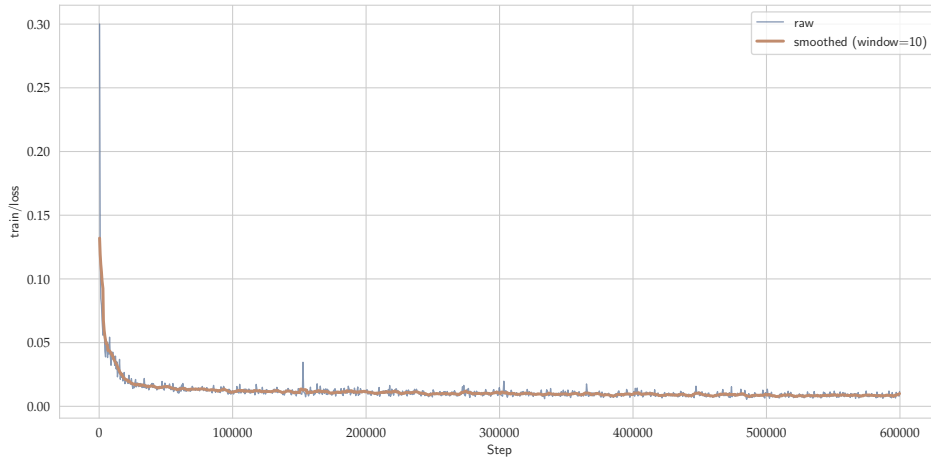


Figure 4: Training loss curves for MotionMillion.

We monitor the training loss and gradient norm curves for our MotionMillion experiments, as shown in Figure 4 and Figure 5. The loss curve shows a smooth and steady decrease throughout training. The gradient norm curve also remains stable with only one spike in the beginning of training, and that’s why we adopt a warm-up learning rate strategy and a single gradient clipping threshold for the entire training process. And at the end of training, both the loss and gradient norm curves are still stable, which suggests that the training process is well-behaved and does not diverge or collapse.

D Implementation Details

D.1 Model Architecture

Our model uses a Diffusion Transformer backbone, while the text encoder varies across datasets.

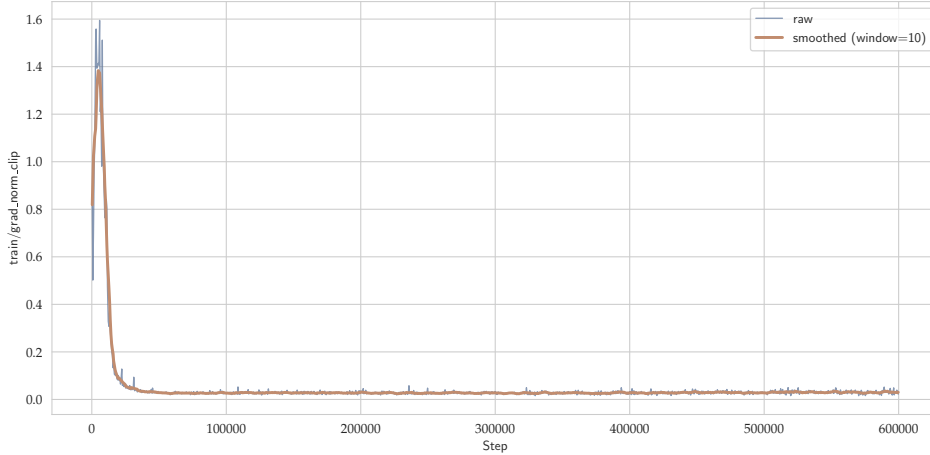


Figure 5: Gradient norm curves for MotionMillion.

For HumanML3D, we use Qwen3-Embedding-0.6B [Zhang et al., 2025] to extract a 1024-dimensional text feature vector. We fuse the text features with the time embedding through an MLP and use the fused representation as the conditioning input to the Diffusion Transformer.

For MotionMillion, we use Qwen3-1.7B [Yang et al., 2025] to extract text features. Unlike Qwen3-Embedding-0.6B, Qwen3-1.7B is a decoder-only large language model. Following recent advances in image generation [Cai et al., 2025, Esser et al., 2024], we therefore adopt a single-stream multi-modal Diffusion Transformer (MM-DiT), where text and motion tokens are concatenated along the sequence dimension and processed as a unified input stream.

D.2 Training Details

Table 7: Training hyperparameters for different model scales.

| Hyperparameter | RMG-base | RMG |
|-------------------------|------------------------|------------------------|
| Input Dim. | 91 | 91 |
| Hidden Dim. | 384 | 1024 |
| No. of Layers | 6 | 24 |
| No. of Heads | 8 | 8 |
| FFN Multiplier | 8 | 4 |
| Max Learning Rate | 1e-4 | 1e-4 |
| Learning Rate Scheduler | Cosine w/ warmup | Cosine w/ warmup |
| Ratio of Warmup Steps | 0.08 | 0.08 |
| Effective Batch Size | $32 \times 8 \times 1$ | $16 \times 8 \times 2$ |
| Training Steps | 150k | 600k |
| Gradient Clipping | 0.5 | 0.5 |

We list the training hyperparameters for different model scales in Table 7. The effective batch size is calculated as the product of the per-device batch size, the number of devices, and the gradient accumulation steps.

D.3 Conversion Functions

We implement two extra conversion functions to convert our representation of human motion to HumanML3D format and MotionMillion format, respectively. The core idea is to first map our

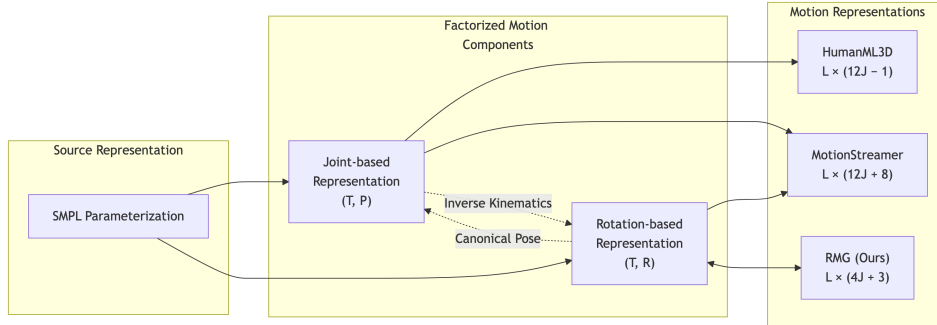


Figure 6: The conversion functions between different motion representations.

representation back to either a rotation-based or a joint-based representation, and then apply the same preprocessing pipeline used by the target format. Figure 6 summarizes these conversion functions.

E Limitations

While our proposed Riemannian Motion Generation framework demonstrates promising results in motion representation and generation, there are several limitations that warrant discussion:

- The Riemannian representation has not been tested on the auto-regressive setting though it’s been a popular stream in recent human motion generation works.
- More conditioning modalities (e.g., music, video) and interactive generation scenarios (e.g., human-object interaction) have not been explored.
- The generation duration is currently limited to 10 seconds (300 frames), and scaling to longer horizons may require larger data collection efforts and more computational resources.
- More body configurations (e.g., hands and face) are not included in the current framework, and extending to these richer configurations may require additional design considerations.
- Motion editing and temporal in-painting are not studied in this work, and it remains to be seen how the Riemannian representation can be adapted to these tasks.

F Broader Impacts

This work may have several positive societal impacts. First of all, it may continue to drive research on large-scale human motion generation. Secondly, it may enable more efficient and scalable motion generation systems, which can be beneficial for various applications such as gaming, virtual reality, and human-computer interaction. Thirdly, it may also inspire future research on geometric representations and low-dimensional manifold modeling in other domains beyond human motion. Lastly, more advanced topics such as world modeling and embodied agents may also benefit from the rapid development of human motion generation.

At the same time, this line of research may also introduce potential risks. More capable human motion generation systems could be misused to synthesize deceptive or misleading human behaviors, and biases or artifacts in the training data may be inherited or amplified in generated motions. In addition, deploying such models in embodied or interactive systems without sufficient safeguards may create safety, fairness, or reliability concerns in downstream applications. We therefore encourage future work to pair technical advances with careful dataset curation, clear disclosure of synthetic content, and application-level safety mechanisms.